Geochemical Perspectives Letters

Growth of upper plate lithosphere controls tempo of arc magmatism: Constraints from Al-diffusion kinetics and coupled Lu-Hf and Sm-Nd chronology

E.J. Chin[1,2*], C.-T.A. Lee[1], J. Blichert-Toft[1,3]

OPEN ACCESS

doi: 10.7185/geochemlet.1503

Abstract

Most magmatism occurs at mid-ocean ridges, where plate divergence leads to decompression melting of the mantle, and at volcanic arcs, where subduction leads to volatile-assisted decompression melting in the hot mantle wedge. While plate spreading and subduction are continuous, arc magmatism, particularly in continental arcs, is characterised by >10-50 Myr intervals of enhanced magmatic activity followed by rapid decline (DeCelles *et al.*, 2009). In some cases, such as the Andes, this pattern has recurred several times (Haschke *et al.*, 2002). Abrupt changes in plate convergence rates and direction (Pilger, 1984) or repeated steepening and shallowing of subducting slabs (Kay and Coira, 2009) have been suggested as triggering flare-ups or terminating magmatism, but such scenarios may not be sufficiently general. Here, we examine the thermal history of deep crustal and lithospheric xenoliths from the Cretaceous Sierra Nevada batholith, California (USA). The deepest samples (~90 km), garnet-bearing spinel peridotites, show cooling-related exsolution of garnet from high-Al pyroxenes originally formed at >1275 °C. Modelling of pyroxene Al diffusion profiles requires rapid cooling from 1275 to 750 °C within ~10 Myr. Also suggesting deep-seated, rapid cooling is a garnet websterite from ~90 km depth with nearly identical Lu-Hf (92.6 ± 1.6 Ma) and Sm-Nd (88.8 ± 3.1 Ma) isochron ages to within error. Thermal modelling shows that this cooling history can be explained by impingement of the base of the Sierran lithosphere against a cold subducting slab at ~90 km depth, precluding cooling by shallowing subduction. Rather, the coincidence of the radiometric ages with the magmatic flare-up (120-80 Ma) suggests that the hot mantle wedge above the subducting slab may have been pinched out by magmatic (± tectonic) thickening of the upper plate, eventually terminating mantle melting. Magmatic flare-ups in continental arcs are thus self-limiting, which explains why continental arc magmatism occurs in narrow time intervals. Convective removal of the deep arc lithosphere can initiate another magmatic cycle.

Received 10 January 2015 | Accepted 13 March 2015 | Published 8 April 2015

1. Department of Earth Science, Rice University, Houston, Texas, USA
2. Department of Earth, Environmental and Planetary Sciences, Brown University, Providence, Rhode Island, USA
* Corresponding author (email: ej3030@gmail.com)
3. Ecole Normale Supérieure de Lyon and Université Lyon 1, Laboratoire de Géologie de Lyon, CNRS UMR 5276, Lyon, France

Introduction

Constraining the thermal and temporal evolution of the deep arc lithosphere is critical to understanding the magmatic evolution of a volcanic arc. The Sierra Nevada batholith is one of only a few places world-wide to study deep crustal and lithospheric evolution of an arc because of the availability of lower crustal and mantle xenoliths (Dodge *et al.*, 1988; Mukhopadhyay and Manton, 1994; Ducea and Saleeby, 1996; Lee *et al.*, 2006, 2007; Chin *et al.*, 2012), which are rare elsewhere. Magmatism in the Sierra Nevada occurred primarily between ~120 and ~80 Ma, peaking at ~95 Ma and terminating abruptly at ~80 Ma (Barton, 1996; Coleman and Glazner, 1997; Ducea, 2001; Paterson *et al.*, 2014). We examined xenoliths from a late Miocene basaltic dike (Big Creek; N 37.208946° W119.264784°) (Fig. 1A). These xenoliths comprise garnet pyroxenites and peridotites and sample a lithospheric section ranging from the mid to lower crust (~33 to ~45 km) into the mantle (~90 km) (Fig. 1B). Sm-Nd ages between 120 and 84 Ma for several pyroxenite xenoliths (Ducea and Saleeby, 1998), along with geochemical data (Lee *et al.*, 2006, 2007), indicate that they represent cumulates left behind by the Cretaceous Sierran granitoids.

Garnet pyroxenite cumulates are volumetrically dominant and can be divided into a low-MgO group composed of garnet-rich clinopyroxenites and a high-MgO group composed of garnet websterites (Lee *et al.*, 2006). The former are interpreted as mid to lower crustal cumulates of an evolved hydrous basalt, whereas the latter are lower crustal and upper mantle cumulates of primitive hydrous basalts, overlapping in final equilibration pressures and therefore interpreted as being interleaved with the spinel and garnet peridotites (Saleeby *et al.*, 2003) (Fig. 1B). Garnet-clinopyroxene rare-earth element (REE) thermobarometry of the low-MgO pyroxenite yields equilibration conditions of ~0.33 GPa and 801 °C (Sun and Liang, 2015) consistent with a mid-crustal origin. In contrast, major element thermobarometry of the high-MgO websterites record equilibration pressures ranging from 1.5 to 3 GPa and temperatures between 700 and 830 °C (Lee *et al.*, 2006). These final P-T conditions are similar to those obtained for the garnet peridotites (2.3 – 3.6 GPa, 651 – 845 °C; Chin *et al.*, 2012).

Although both garnet peridotites and high-MgO websterites achieved similar high final pressures and low final temperatures, high-Al orthopyroxene cores in both rock types point to initially high temperatures. In high-MgO websterites, orthopyroxene cores record temperatures of ~1100 °C, supporting an origin as magmatic cumulates precipitated from primary basaltic liquids (Lee *et al.*, 2006; Supplementary Information). Mineral and bulk rock compositions of the garnet peridotites indicate that their protoliths were spinel peridotites that were melt-depleted at shallow (1 GPa) depths. These spinel peridotites were subsequently refertilised and transported to cold and deep final conditions in the garnet stability field (Chin *et al.*, 2012, 2014). Temperatures corresponding to melting, and thus initial temperatures, can be obtained using Fe-Mg partitioning between peridotite and melt (Lee and Chin, 2014). Melting temperatures for the garnet peridotites fall between 1300 and 1400 °C (Chin *et al.*, 2012). These initial

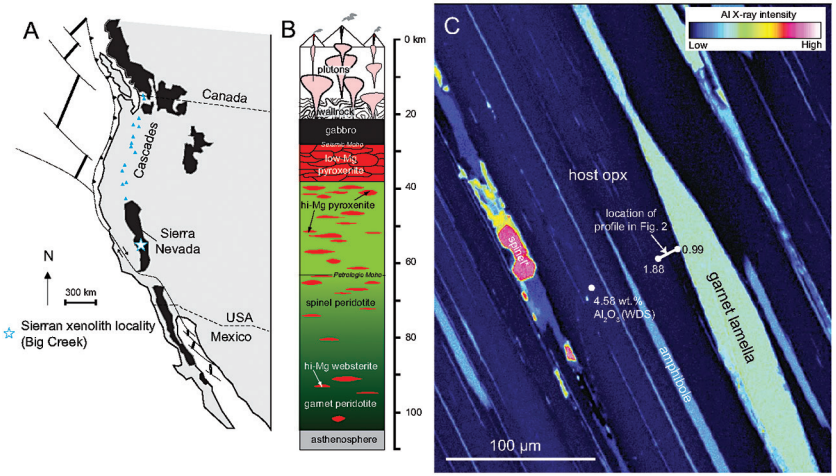

Figure 1 **(A)** Sample locality map. **(B)** Vertical architecture of the lithosphere beneath the central Sierra Nevada as sampled by xenoliths (see text for references). **(C)** Wavelength-dispersive (WDS) elemental map of Al intensity in an orthopyroxene containing garnet and amphibole lamellae in garnet peridotite 1026V from 3 GPa (~90 km). Spots labelled as wt.% Al_2O_3 correspond to individual, quantitative WDS spot measurements.

temperatures are consistent with the high Al in orthopyroxene away from contact with exsolved garnet lamellae (Fig. 1C). For example, in the profile shown in Figure 1C, the distal Al_2O_3 of 1.88 wt. % would correspond to 1275 °C at 3 GPa using the garnet-orthopyroxene thermobarometer of Harley and Green (1982).

For this study, one garnet peridotite (1026V) containing well-developed garnet exsolution lamellae was selected for modelling diffusion kinetics. Garnet pyroxenites were selected for Lu-Hf and Sm-Nd chronology owing to their high modal abundances of garnet (25–50 %) and clinopyroxene (50–60 %) (garnet peridotites provided insufficient quantities of separable garnet for dating). We chose a low-MgO pyroxenite (BCX; final T of 801 °C and final P of 0.33 GPa using the REE garnet-clinopyroxene thermobarometer of Sun and Liang (2015)), a high-MgO websterite (BC98-5, average final T of 702 °C and average final P of 2.4 GPa), and a high-MgO amphibole-bearing websterite (BC98-7, average final T of 710 °C and average final P of 1.6 GPa). Sample BC98-7 has an amphibole vein replacing pyroxene and hence was selected deliberately to provide insight into the timing of hydrous metasomatism.

Methods

High spatial resolution elemental data on sample 1026V were determined by field emission electron microprobe analyser (EPMA) using wavelength-dispersive spectroscopy (WDS) with operating conditions at 15 kV accelerating voltage and

5 nA probe current using the JEOL JXA-8530 F 'Hyperprobe' at Yale University. Core and rim mineral compositions in garnet pyroxenites were determined by WDS (15 kV, 20 nA) on the CAMECA SX-50 at Texas A&M University. Typical spot sizes on both electron probes were 1 to 1.5 µm.

Thermobarometry was based on mineral major and trace element compositions published in Lee *et al.* (2006) and Chin *et al.* (2012) and the data reported in this study.

For Sm-Nd and Lu-Hf isotopic analysis, clean garnet and clinopyroxene were separated by hand. Between 60 and 680 mg of garnet, clinopyroxene, and whole-rock powders were acid-digested in Parr bombs. Sm, Nd, Lu and Hf were separated by ion-exchange column chromatography and their isotopic compositions measured by multiple-collector inductively coupled plasma mass spectrometry following the procedures outlined in Blichert-Toft *et al.* (1997, 2002), Blichert-Toft (2001), and Blichert-Toft and Puchtel (2010). Sm, Nd, Lu and Hf concentrations were determined by isotope dilution using >98 % pure mixed ^{149}Sm-^{150}Nd and ^{176}Lu-^{180}Hf spikes added to the samples at the outset of dissolution. Data and further details of the analytical procedures are in the Supplementary Information.

Al diffusion modelling was done by finite-difference, allowing for temperature-dependent diffusivity and boundary conditions. Magnitude of time-steps were adapted with temperature and diffusivity to maintain numerical closure. Thermal modelling was based on conventional finite-difference models of conduction. Additional details on modelling set up and parameters are provided in the Supplementary Information.

Results

Al-depletion haloes in orthopyroxene. Field emission electron microprobe measurements show that BC98-7, BC98-5, and 1026V have orthopyroxenes zoned from high-Al cores to low-Al rims (Supplementary Information). In particular, Al in orthopyroxene porphyroclasts becomes depleted towards the contacts with garnet exsolution lamellae. Al-depletion halo thicknesses in orthopyroxene adjacent to the garnet lamellae range from 5-20 µm and are positively correlated with garnet lamellae thickness, confirming that garnet formed by exsolution from an original high-Al, high-temperature pyroxene (Chin *et al.*, 2012). The Al concentration profiles exhibit strong curvature due to 50 % depletion within the first ~5 µm from the contact followed by only moderate (15 %) depletion 5-20 µm from the contact (Fig. 2).

Diffusion modelling. The thickness and shape of the Al-depletion halo in garnet peridotite-hosted pyroxenes in sample 1026V can be used to constrain the cooling rate of the xenolith during its residence in the deep lithosphere. We numerically solved the 1-D chemical diffusion equation with temperature-dependent diffusivity and temperature-dependent boundary conditions at the

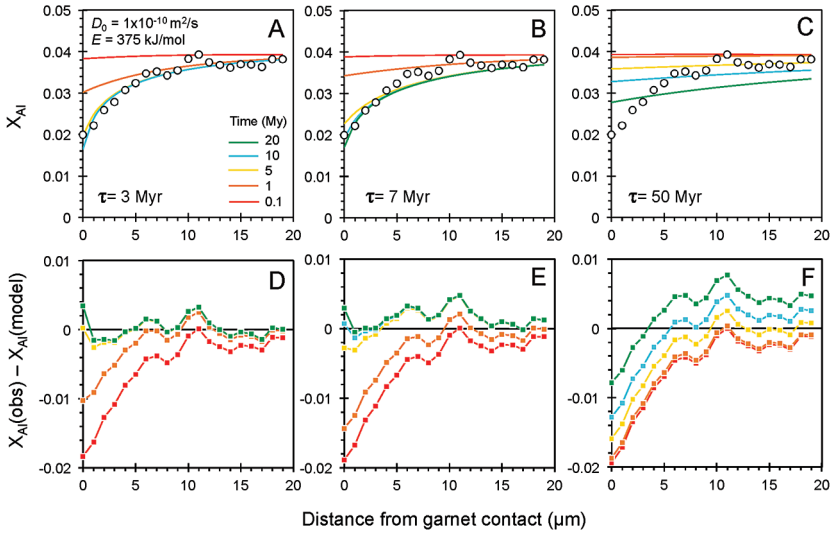

Figure 2 Orthopyroxene Al diffusion modelling of the Al halo transect shown in Figure 1C. Quantitative WDS spot analyses along the transect are plotted as white circles. **(A-C)** show diffusion profiles at selected times (0.1, 1, 5, 10, 20 Ma) using an activation energy *E* of 375 kJ/mol and D_0 = 10^{-10} m^2/s. Three different cooling scenarios are shown, with e-fold timescales of cooling τ of 3, 7, and 50 Myr. **(D-F)** show the residual (X_{Al}(observed) – X_{Al}(modelled)) as a function of distance for each of the models, where X_{Al} = atomic Al/2, and Al is the number of cations in the formula for orthopyroxene on a 6 oxygen basis.

garnet-pyroxene interface for a range of possible cooling histories (see Supplementary Information for details on the modelling approach). We assumed that cooling and associated garnet exsolution occurred isobarically at the final recorded equilibration pressures in 1026V (3 GPa). We adopted an initial temperature of 1275 °C, corresponding to the maximum Al_2O_3 content of 1.88 wt. % far from the garnet contact (Fig. 1C, Table S-1). We also explored a lower initial temperature of 1100 °C, corresponding to the high-Al cores in the high-MgO websterites to evaluate whether our chemical diffusion modelling could be used to interpret the thermal evolution of the coexisting websterites, which show similar Al zoning in orthopyroxenes. For the final temperature, we use 750 °C, corresponding to mineral rim compositions and thus final equilibration temperatures of both peridotites and websterites. To explore the range of possible cooling histories, we assumed that temperature decreased exponentially from 1275 to 750 °C over e-fold timescales τ ranging from 3, 7, and 50 Myr. The temperature-dependent boundary condition was determined by parameterising the garnet-orthopyroxene thermobarometer of Harley and Green (1982) at 3 GPa.

No experimental data are available for Al diffusion in orthopyroxene, but experiments on REE^{3+} diffusion in orthopyroxene may provide a suitable analogue for estimating the parameters of diffusivity *D*, that is, $D = D_0\exp(-E/RT)$, where D_0 is the pre-exponent (m^2/s), *E* is the activation energy (kJ/mol), *R* is the gas constant, and *T* is temperature (K). Cherniak and Liang (2007) obtained a D_0 of 1.2×10^{-7} m^2/s and *E* of 369 kJ/mol after averaging all experimental data for REE and Y diffusion in orthopyroxene. They showed that *E* does not vary with cation radius, so *E* for Al diffusivity is assumed to be similar. We therefore adopted a nominal value of 375 kJ/mol for *E* though other values are explored in the Supplementary Information. D_0, however, is expected to vary with ionic radius based on experiments on clinopyroxene (Van Orman *et al.*, 2001), but the relationship is not clear for experiments on orthopyroxene. We thus varied D_0 from 10^{-7} to 10^{-12} m^2/s over the three cooling scenarios and evaluated which combination of parameters best match the magnitude and curvature of the Al-depletion halo. For a given cooling scenario, as D_0 increases, the modelled profiles progressively flatten because the higher the D_0, the faster the Al diffusion front can propagate into the pyroxene. For a given D_0, decreasing the cooling rate decreases curvature because longer cooling times allow more time for diffusion.

In Figure 2A-C, we show model results of Al profiles, including residuals (Fig. 2D-F), versus elapsed time. The parameters used for the model results in Figure 2 were D_0 of 10^{-10} m^2/s, *E* of 375 kJ/mol, τ of 3, 7, and 50 Myr, starting temperature of 1275 °C, and final temperature of 750 °C (results of models using starting temperature of 1100 °C are shown in the Supplementary Information). The best fit models require closure of the system for Al within 5 Myr for τ of 3 Myr and within 10 Myr for τ of 7 Myr. Model results for other D_0s give poor fits or require unreasonable cooling rates to achieve a good fit. For example, the only model using D_0 of 10^{-11} m^2/s consistent with the observed Al profile requires τ of 50 Myr and closure at 100 Myr, while it is clear that a cooling duration of 100 Myr for the Sierran deep lithosphere is unacceptably long given the well-constrained magmatic peak at ~95 Ma (Paterson *et al.*, 2014) and closure of garnet websterite Sm-Nd ages between 81 and 89 Ma (discussed below). The most robust models are for D_0 of 10^{-10} m^2/s and τ of 3-7 Myr and indicate that the base of the Sierran lithosphere (90 km) cooled from 1275 to 750 °C within 10 Myr. We note that if we had assumed a lower initial temperature (1100 °C) corresponding to the maximum Al in orthopyroxene cores in the garnet websterites, we obtain a similar result consistent with cooling within 10 Myr at fast cooling rates (Supplementary Information).

Coupled Lu-Hf and Sm-Nd chronology. Additional constraints on the cooling history of the Sierran lithosphere come from coupled Lu-Hf and Sm-Nd chronology. Although the closure temperatures of the Lu-Hf and Sm-Nd systems depend on many factors, such as cooling rate, grain size, and diffusion parameters, which are not always well constrained in texturally complex systems, it is known that the Lu-Hf system closes at higher temperatures than the Sm-Nd system (Kylander-Clark *et al.*, 2007; Cheng *et al.*, 2008). The slopes of lines

regressed through garnet, clinopyroxene, and whole-rock data on $^{176}Hf/^{177}Hf$ versus $^{176}Lu/^{177}Hf$ and $^{143}Nd/^{144}Nd$ versus $^{147}Sm/^{144}Nd$ diagrams yield ages broadly coeval with magmatism (120-85 Ma) in the Sierra Nevada (Fig. 3). For the deep high-MgO websterite (BC98-5), Lu-Hf and Sm-Nd ages are identical to within analytical uncertainties (92.6 ± 1.6 Ma and 88.8 ± 3.1 Ma, respectively). For the shallow low-MgO pyroxenite (BCX), the Lu-Hf age is considerably older (107.9 ± 1.4 Ma) than the Sm-Nd age (84.0 ± 4.1 Ma), the former coinciding with the main peak of arc magmatism as inferred from the ages of plutons and the latter coinciding with the tail end of the magmatic flare-up. For the amphibole-bearing sample BC98-7, the Lu-Hf age is younger (60.8 ± 3.2 Ma) than the Sm-Nd age (81.0 ± 2.0 Ma), the latter of which is consistent within the quoted uncertainties with the Sm-Nd ages of the other samples.

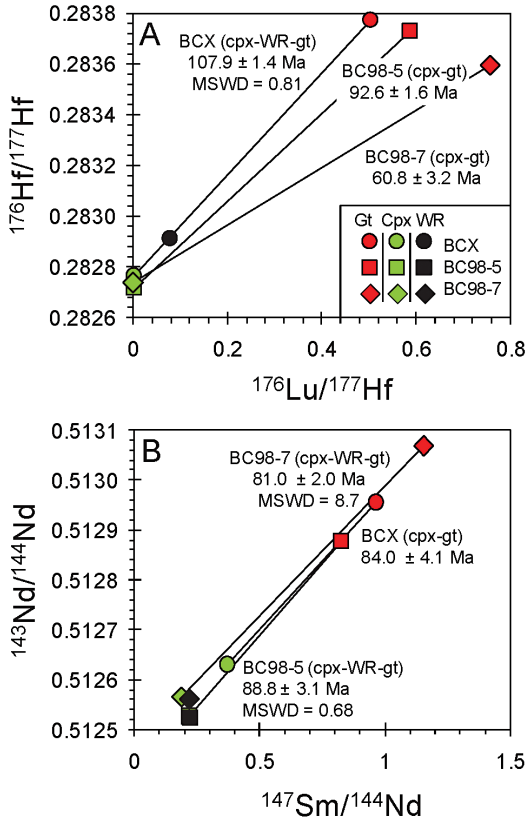

Figure 3 **(A)** Lu-Hf and **(B)** Sm-Nd isochrons of Sierran garnet pyroxenite xenoliths. Isochrons were calculated using a MatLab least-squares software by F. Albarède (version 6.0, 2013).

Discussion

The rapid cooling rates of the deep Sierran lithosphere inferred from Al-diffusion modelling are consistent with the near-identical Lu-Hf and Sm-Nd isochron ages of the deep garnet websterite BC98-5. The Lu-Hf and Sm-Nd ages of BC98-5 constrain cooling between the two closure temperatures to be within 5 Myr. Thus, diffusion modelling and chronology suggest that the base of the Sierran lithosphere remained hot until ~92 Ma (the Lu-Hf age), after which it cooled rapidly. In contrast, the coincidence of shallow pyroxenite BCX's Lu-Hf age with pluton ages suggests that the 108 Ma Lu-Hf age simply may represent a crystallisation age during passage of magmas in the cold shallow parts of the lithosphere (<45 km) (Fig. 4A, B). BCX's young Sm-Nd age, however, is identical to ages from the base of the lithosphere as represented by BC98-5, indicating that, although BCX crystallised at 108 Ma, it cooled slowly after crystallisation, passing through the Sm-Nd closure temperature at roughly the same time as the deep lithosphere as recorded by BC98-5. This suggests that the entire lithosphere, as represented by the shallow low-MgO pyroxenite and the deep high-MgO websterite and peridotites, experienced cooling at around 92 Ma, just after the peak of arc magmatism. The Lu-Hf and Sm-Nd systematics of amphibole-bearing BC98-7 from the base of the Sierran lithosphere is more perplexing because, although its Sm-Nd age of 81 Ma is within error of Sierran magmatism, its Lu-Hf age is much younger (60.8 Ma). However, we note that the chemical dissimilarity between rare earth element Lu and high field strength element Hf allows for more extreme parent/daughter fractionation in fluid-mediated processes, whereas Sm and Nd, two neighbouring light rare earth elements, are more difficult to fractionate owing to their similar chemical behaviour under all conditions. Thus, the young Lu-Hf age of BC98-7 may reflect resetting by fluid metasomatism of the deep lithosphere continuing well after arc magmatism ended.

One scenario that may explain the rapid cooling inferred at the base of the Sierran lithosphere is if the lithosphere impinged against a cold subducting plate. To satisfy the age constraints, such impingement would have had to occur at ~92 Ma and the depth at which the impingement occurred must have been greater than the deepest xenolith equilibration pressures of ~3 GPa (~100 km). To simulate this scenario, we modelled thermal diffusion in a 100-km thick lithosphere that is instantaneously juxtaposed against a cold slab at 100 km depth. We assume the deepest part of the Sierran lithosphere, represented by interleaved high-MgO garnet websterite and garnet peridotite, to be initially 1300 °C, decreasing with decreasing depth to a surface temperature of 25 °C. We take the temperature of the top of a slab to be 750 °C, based on Syracuse *et al.* (2010). Cooling histories are shown in Figures 4C and 4D, where it can be seen that the deepest part of the lithosphere cools the fastest. In Figure 4D, the cooling histories determined from Al-diffusion kinetics, using 1275 °C as the initial temperature and 750 °C as the final temperature (Fig. 2), are also compared with the cooling histories from the conductive cooling model. Thus, Al-diffusion kinetics, coupled Sm-Nd

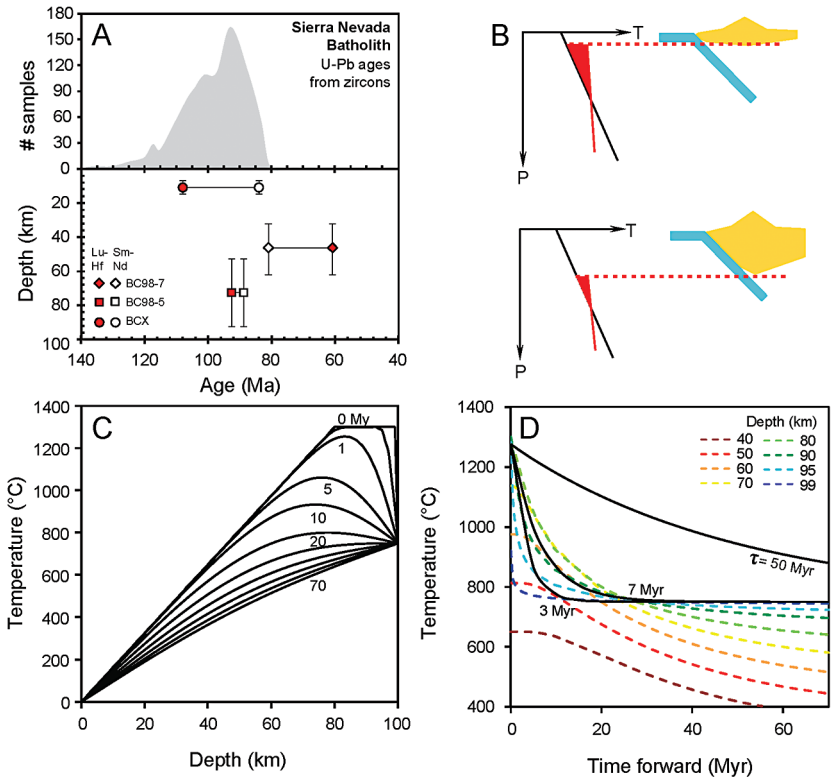

Figure 4 **(A) Top panel:** U-Pb zircon ages from the Sierra Nevada Batholith (Paterson *et al.*, 2014) showing a major peak at ~95 Ma. **Bottom panel:** Thermobarometrically constrained depth versus radiometric age of Sierran pyroxenite xenoliths. The vertical bars represent the range of final P, T recorded by several mineral rim pairs in each xenolith (except for BCX, where average REE concentrations were used); the symbols represent the average P, T. **(B)** Cartoon illustrating the formation of shallow low-MgO pyroxenite (top) and deep high-MgO websterite (bottom). **(C)** Temperature versus depth diagram showing the initial condition of conductive cooling modelling of a 100-km thick lithosphere at 0 Myr (initial condition) and re-equilibration to a new ambient geotherm after 70 Myr. Thermal diffusivity is 10^{-6} m^2/s. **(D)** Temperature versus time diagram of depth slices ranging from 40 to 99 km. Superimposed on the diagram are the three cooling scenarios evaluated in the Al-diffusion modelling.

and Lu-Hf chronology, and thermal modelling all independently lead to the same conclusion that the base of the Sierran lithosphere cooled from >1250 °C to 750 °C in <10 Myr, just after the peak of arc magmatism.

Although cooling of the deep Sierran lithosphere by slab "refrigeration" has been suggested previously, shallowing of the slab dip typically has been invoked (Dickinson and Snyder, 1978; Dumitru *et al.*, 1991). However, the presence of

cold xenoliths at ~100 km depth requires, instead, that the Sierran arc lithosphere thickened downward and impinged upon a normally dipping slab, ~100 km beneath the arc front. The coincidence of thickening with the peak of arc magmatism suggests that crustal thickening must have, in part, been driven by magmatic additions to the crust (Flowers *et al.*, 2005; Jagoutz, 2010). We therefore propose that magmatic thickening may be a key mechanism that modulates the tempo of arc magmas, specifically the abrupt cessation of magmatism observed in many continental arcs. With progressive magmatic additions to the crust, the upper plate thickens, eventually impinging against the cold subducting lower plate and terminating magmatism. In other words, magmatic flare-ups, whatever their origin, cannot be sustained for long periods of time if magmatism leads to thickening. The ability for magmatism to thicken the upper plate depends on the stress state of the upper plate (Karlstrom *et al.*, 2014). In many island arcs, the upper plate is in extension, which could compensate for magmatic thickening. In contrast, the upper plate in continental arcs tends to be in compression, adding to the effects of magmatic thickening (DeCelles, 2004; Paterson *et al.*, 2011). Because of these intimate relationships between magmatism and crustal thickness, we predict that continental arc magmatism should rise and fall over tens of millions of years, while magmatism in island arcs should be long-lived.

Acknowledgements

We thank Simon Harley and Chenguang Sun for thorough and critical reviews. We also thank Wenrong Cao and Scott Paterson for insightful discussions while writing the manuscript. This work was supported by the US-NSF grant EAR-1119315 to C.-T.A. Lee, a Geological Society of America Grant-in-Aid and the Martha Lou Broussard Fellowship to E.J. Chin, and the French Agence Nationale de la Recherche grant ANR-10-BLAN-0603 (M&Ms – Mantle Melting – Measurements, Models, Mechanisms) to J. Blichert-Toft.

Editor: Bruce Watson

Additional Information

Supplementary Information accompanies this letter at http://www.geochemicalperspectivesletters.org/article1503

Reprints and permission information is available online at http://www.geochemicalperspectivesletters.org/copyright-and-permissions

Cite this letter as: Chin, E.J., Lee, C.-T.A., Blichert-Toft, J. (2015) Growth of upper plate lithosphere controls tempo of arc magmatism: Constraints from Al-diffusion kinetics and coupled Lu-Hf and Sm-Nd chronology. *Geochem. Persp. Let.* 1, 20-32.

Author Contributions

E.J. Chin collected the electron microprobe data; J. Blichert-Toft and E.J. Chin did the Lu-Hf and Sm-Nd isotope measurements; E.J. Chin and C.-T.A. Lee modelled the Al and thermal diffusion; and E.J. Chin wrote the manuscript with help from C.-T.A. Lee and J. Blichert-Toft. All authors discussed the results and commented on the manuscript.

References

Barton, M.D. (1996) Granitic magmatism and metallogeny of southwestern North America. In: Brown, M., Candela, P.A., Peck, D.L., Stephens, R.J.W., Zen, E.-A. (Eds.) *The Third Hutton Symposium on the Origin of Granites and Related Rocks*. GSA Special Papers, 261-280.

Blichert-Toft, J. (2001) On the Lu-Hf Isotope Geochemistry of Silicate Rocks. *Geostandards Newsletter* 25, 41-56.

Blichert-Toft, J., Puchtel, I.S. (2010) Depleted mantle sources through time: Evidence from Lu-Hf and Sm-Nd isotope systematics of Archean komatiites. *Earth and Planetary Science Letters* 297, 598-606.

Blichert-Toft, J., Chauvel, C., Albarède, F. (1997) Separation of Hf and Lu for high-precision isotope analysis of rock samples by magnetic sector-multiple collector ICP-MS. *Contributions to Mineralogy and Petrology* 127, 248-260.

Blichert-Toft, J., Boyet, M., Télouk, P., Albarède, F. (2002) $^{147}Sm/^{143}Nd$ and $^{176}Lu/^{176}$ Hf in eucrites and the differentiation of the HED parent body. *Earth and Planetary Science Letters* 204, 167-181.

Cheng, H., King, R.L., Nakamura, E., Vervoort, J.D., Zhou, Z. (2008) Coupled Lu–Hf and Sm–Nd geochronology constrains garnet growth in ultra-high-pressure eclogites from the Dabie orogen. *Journal of Metamorphic Geology* 26, 741-758.

Cherniak, D.J., Liang, Y. (2007) Rare earth element diffusion in natural enstatite. *Geochimica et Cosmochimica Acta* 71, 1324-1340.

Chin, E.J., Lee, C.-T.A., Luffi, P., Tice, M. (2012) Deep Lithospheric Thickening and Refertilization beneath Continental Arcs: Case Study of the P, T and Compositional Evolution of Peridotite Xenoliths from the Sierra Nevada, California. *Journal of Petrology* 53, 477-511.

Chin, E.J., Lee, C.-T.A., Barnes, J.D. (2014) Thickening, refertilization, and the deep lithosphere filter in continental arcs: Constraints from major and trace elements and oxygen isotopes. *Earth and Planetary Science Letters* 397, 184-200.

Coleman, D.S., Glazner, A.F. (1997) The Sierra Crest Magmatic Event: Rapid Formation of Juvenile Crust during the Late Cretaceous in California. *International Geology Review* 39, 768-787.

DeCelles, P.G. (2004) Late Jurassic to Eocene evolution of the Cordilleran thrust belt and foreland basin system, western U.S.A. *American Journal of Science* 304, 105-168.

DeCelles, P.G., Ducea, M.N., Kapp, P., Zandt, G. (2009) Cyclicity in Cordilleran orogenic systems. *Nature Geoscience* 2, 251-257.

Dickinson, W.R., Snyder, W.S. (1978) Plate tectonics of the Laramide orogeny. In: Matthews, V. (Ed.) *Laramide folding associated with basement block faulting in the Western United States*. Geological Society of America Memoir 151, 355-366.

Dodge, F.C.W., Lockwood, J.P., Calk, L.C. (1988) Fragments of the mantle and crust from beneath the Sierra Nevada batholith: Xenoliths in a volcanic pipe near Big Creek, California. *Geological Society of America Bulletin* 100, 938-947.

Ducea, M.N. (2001) The California Arc: Thick Granitic Batholiths, Eclogitic Residues, Lithospheric-Scale Thrusting, and Magmatic Flare-Ups. *GSA Today* 11, 4-10.

Ducea, M.N., Saleeby, J.B. (1996) Buoyancy sources for a large, unrooted mountain range, the Sierra Nevada, California: Evidence from xenolith thermobarometry. *Journal of Geophysical Research* 101, 8229-8244.

Ducea, M.N., Saleeby, J.B. (1998) The age and origin of a thick mafic–ultramafic keel from beneath the Sierra Nevada batholith. *Contributions to Mineralogy and Petrology* 133, 169-185.

Dumitru, T.A., Gans, P.B., Foster, D.A., Miller, E.L. (1991) Refrigeration of the western Cordilleran lithosphere during Laramide shallow-angle subduction. *Geology* 19, 1145-1148.

Flowers, R.M., Bowring, S.A., Tulloch, A.J., Klepeis, K.A. (2005) Tempo of burial and exhumation within the deep roots of a magmatic arc, Fiordland, New Zealand. *Geology* 33, 17-20.

Harley, S.L., Green, D.H. (1982) Garnet-orthopyroxene barometry for granulites and peridotites. *Nature* 300, 697-701.

Haschke, M., Siebel, W., Günther, A., Scheuber, E. (2002) Repeated crustal thickening and recycling during the Andean orogeny in north Chile (21-26 S). *Journal of Geophysical Research: Solid Earth (1978-2012)* 107, ECV 6-1-ECV 6-18.

Jagoutz, O. (2010) Construction of the granitoid crust of an island arc. Part II: a quantitative petrogenetic model. *Contributions to Mineralogy and Petrology* 160, 359-381.

Karlstrom, L., Lee, C.-T.A., Manga, M. (2014) The role of magmatically driven lithospheric thickening on arc front migration. *Geochemistry, Geophysics, Geosystems* 15, 2655-2675.

Kay, S.M., Coira, B.L. (2009) Shallowing and steepening subduction zones, continental lithospheric loss, magmatism, and crustal flow under the Central Andean Altiplano-Puna Plateau. *Backbone of the Americas: shallow subduction, plateau uplift, and ridge and terrane collision* 204, 229-259.

Kylander-Clark, A.R., Hacker, B.R., Johnson, C.M., Beard, B.L., Mahlen, N.J., Lapen, T.J. (2007) Coupled Lu-Hf and Sm-Nd geochronology constrains prograde and exhumation histories of high-and ultrahigh-pressure eclogites from western Norway. *Chemical Geology* 242, 137-154.

Lee, C.-T.A., Chin, E.J. (2014) Calculating melting temperatures and pressures of peridotite protoliths: Implications for the origin of cratonic mantle. *Earth and Planetary Science Letters* 403, 273-286.

Lee, C.-T.A., Cheng, X., Horodyskyj, U. (2006) The development and refinement of continental arcs by primary basaltic magmatism, garnet pyroxenite accumulation, basaltic recharge and delamination: insights from the Sierra Nevada, California. *Contributions to Mineralogy and Petrology* 151, 222-242.

Lee, C.-T.A., Morton, D.M., Kistler, R.W., Baird, A.K. (2007) Petrology and tectonics of Phanerozoic continent formation: From island arcs to accretion and continental arc magmatism. *Earth and Planetary Science Letters* 263, 370-387.

Mukhopadhyay, B., Manton, W.I. (1994) Upper-Mantle Fragments from Beneath the Sierra Nevada Batholith: Partial Fusion, Fractional Crystallization, and Metasomatism in a Subduction Related Ancient Lithosphere. *Journal of Petrology* 35, 1417-1450.

Paterson, S.R., Okaya, D., Memeti, V., Economos, R., Miller, R.B. (2011) Magma addition and flux calculations of incrementally constructed magma chambers in continental margin arcs: Combined field, geochronologic, and thermal modeling studies. *Geosphere* 7, 1439-1468.

Paterson, S.R., Memeti, V., Anderson, L., Cao, W., Lackey, J.S., Putirka, K.D., Miller, R.B., Miller, J.S., Mundil, R. (2014) Day 6: Overview of arc processes and tempos. *Field Guides* 34, 87-116.

Pilger, R.H. (1984) Cenozoic plate kinematics, subduction and magmatism: South American Andes. *Journal of the Geological Society* 141, 793-802.

Saleeby, J., Ducea, M., Clemens-Knott, D. (2003) Production and loss of high-density batholithic root, southern Sierra Nevada, California. *Tectonics* 22, 1064.

Sun, C., Liang, Y. (2015) A REE-in-garnet-clinopyroxene thermobarometer for eclogites, granulites and garnet peridotites. *Chemical Geology* 393-394, 79-92.

Syracuse, E.M., van Keken, P.E., Abers, G.A. (2010) The global range of subduction zone thermal models. *Physics of the Earth and Planetary Interiors* 183, 73-90.

Van Orman, J., Grove, T., Shimizu, N. (2001) Rare earth element diffusion in diopside: influence of temperature, pressure, and ionic radius, and an elastic model for diffusion in silicates. *Contributions to Mineralogy and Petrology* 141, 687-703.

Growth of upper plate lithosphere controls tempo of arc magmatism: Constraints from Al-diffusion kinetics and coupled Lu-Hf and Sm-Nd chronology

E.J. Chin[1,2*], C.-T.A. Lee[1], J. Blichert-Toft[1,3]

Supplementary Information

The Supplementary Information includes:

- Supplementary Data
- Supplementary Methods
- Figures S-1 to S-9
- Tables S-1 to S-5
- Supplementary References

Supplementary Data

Mineral compositions and petrography of Sierran pyroxenites and garnet peridotite 1026V

Our study investigated four Sierran xenoliths. Of these, one xenolith is a garnet peridotite (1026V). Major element compositions of the transect shown in Figure 1C are reported in Table S-1. The remaining three xenoliths are pyroxenites: one low-MgO (<15 wt.% MgO) garnet clinopyroxenite (BCX) and two high-MgO (>15 wt.% MgO) garnet websterites (BC98-5, BC98-7). Whole-rock major element and trace element geochemistry, major and trace element mineral compositions, and petrography for 1026V were previously published in Lee *et al.* (2001), Lee (2005),

1. Department of Earth Science, Rice University, Houston, Texas, USA
2. Department of Earth, Environmental and Planetary Sciences, Brown University, Providence, Rhode Island, USA
* Corresponding author (email: ej3030@gmail.com)
3. Ecole Normale Supérieure de Lyon and Université Lyon 1, Laboratoire de Géologie de Lyon, CNRS UMR 5276, Lyon, France

and Chin *et al.* (2012). For microphotographs and additional details on petrography and textures in 1026V, the reader is referred to Chin *et al.* (2012). Here, we focus on the garnet exsolution within orthopyroxene texture in 1026V and its utility in Al diffusion modelling. We also report new electron microprobe measurements of minerals in BCX, BC98-5, and BC98-7. In Figure S-1 we show that the two high-MgO websterites BC98-5 and BC98-7 have orthopyroxenes zoned from high-Al cores to low-Al rims, similar to previously observed Al zonation in 1026V. All probe data are reported in Tables S2 – S4.

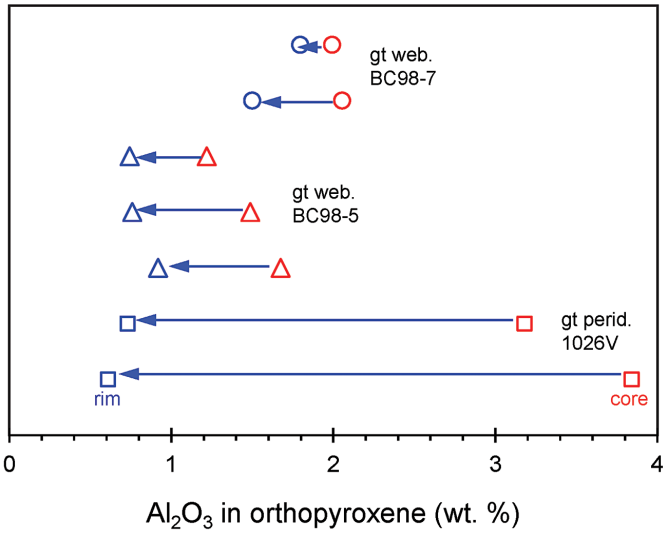

Figure S-1 Al_2O_3 (wt. %) in orthopyroxene cores and rims in garnet websterites and garnet peridotite. Cores have higher Al contents.

Supplementary Methods

a. Lu-Hf and Sm-Nd Isotope Geochemistry

For combined Sm-Nd and Lu-Hf isotope analyses, garnet and clinopyroxene were separated from the pyroxenites by first gently disaggregating ~5 cm whole-rock chunks using a rock hammer. Samples were wrapped in paper towels to minimise contact with the metal hammer, and only the freshest, interior gravel-size pieces were selected for further hand crushing in an agate mortar. Samples were then sieved for grain sizes between 250 to 500 µm. From this fraction, minerals were handpicked under a binocular microscope. Owing to ubiquitous kelyphite rims (Figs. S2-S4), garnets were repeatedly re-crushed by hand in agate after several

rounds of picking to separate out a "clean", kelyphite-free fraction and a "dirty", kelyphite-bearing fraction. Representative "clean" mineral separates are shown in Figure S-5.

While every effort was made to separate as much "clean" garnet as possible, the ubiquitous nature of kelyphite made it difficult for BC98-5. For this sample, kelyphite-bearing garnet therefore was analysed. The presence of kelyphite rims apparently did not disturb the Sm-Nd and Lu-Hf ages – garnet, clinopyroxene, and the whole-rock defined a 3-point Sm-Nd isochron of 88.8 ± 3.1 Ma (MSWD = 0.68) and a 2-point Lu-Hf "isochron" of 92.6 ± 1.6 Ma.

Prior to sample dissolution, mineral separates were cleaned in dilute HCl, ultrasonicated for several hours, and rinsed with ultrapure de-ionised water. All sample dissolution procedures and Sm, Nd, Lu, and Hf chemical separation and isotopic analysis were carried out at the Ecole Normale Supérieure in Lyon. After dissolution in Parr bombs, Sm, Nd, Lu, and Hf were separated from ca. 60-680 mg sized aliquots (depending on degree of sample depletion and sample availability) of garnet and clinopyroxene separates and whole-rock powders by ion-exchange column chromatography, and measured for their isotopic compositions by MC-ICP-MS (Nu Plasma 500 HR) coupled with a desolvating nebuliser DSN-100 according to the procedures of Blichert-Toft *et al.* (1997, 2002), Blichert-Toft (2001), and Blichert-Toft and Puchtel (2010).

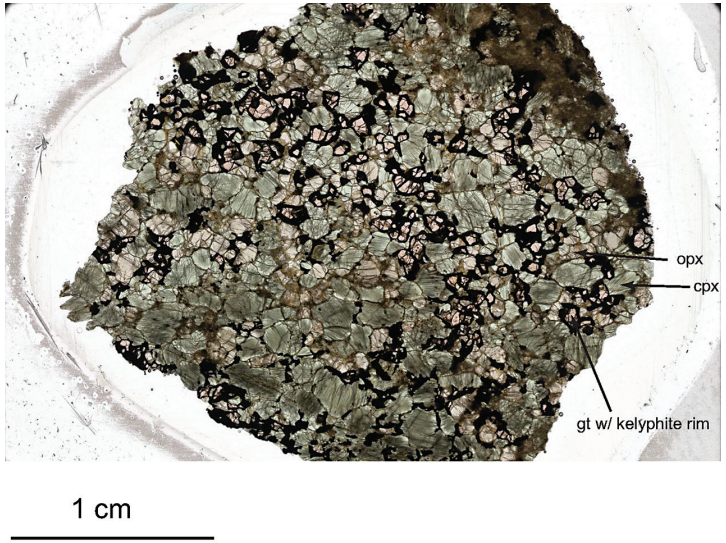

Figure S-2 Plane-polarised light photograph of thick section (~200 µm) of high-MgO websterite BC98-5.

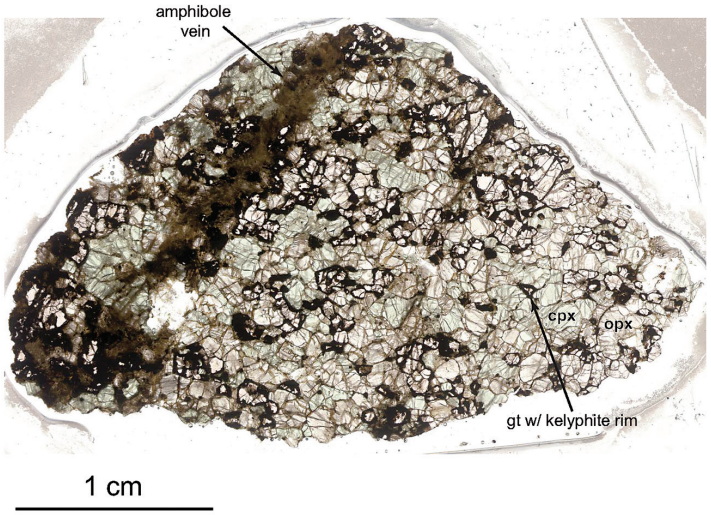

Figure S-3 Plane-polarised light photograph of thick section (~200 µm) of high-MgO websterite BC98-7.

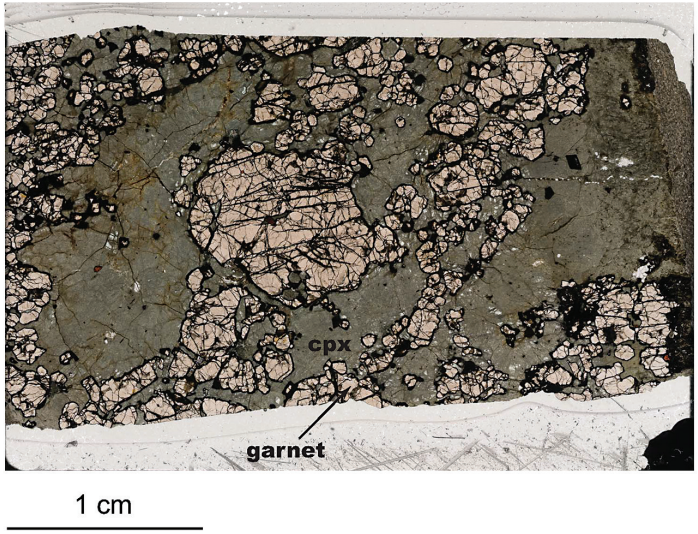

Figure S-4 Plane-polarised light photograph of thick section (~200 µm) of low-MgO garnet clinopyroxenite BCX.

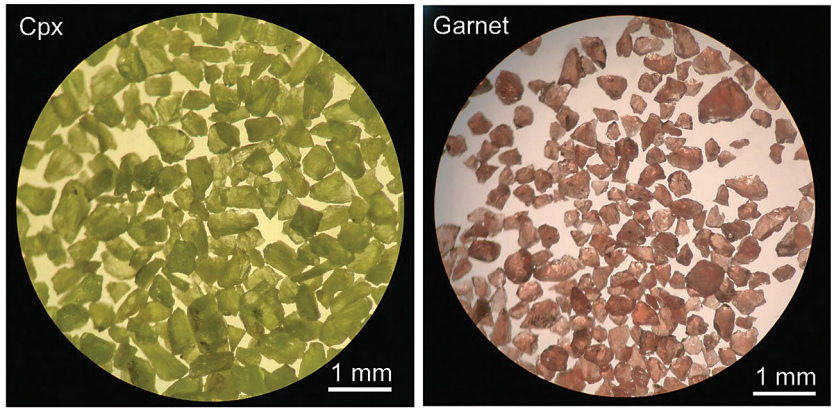

Figure S-5 Representative "clean" clinopyroxene and garnet separates from BC98-5.

Samarium, Nd, Lu, and Hf concentrations were determined by isotope dilution using >98 % pure mixed ^{149}Sm-^{150}Nd and ^{176}Lu-^{180}Hf spikes added to the samples at the outset of the dissolution procedure. The "Rennes" in-house Nd and JMC-475 Hf standards were analysed systematically every one or two samples to monitor machine performance and allow for sample-standard bracketing of the unknowns. The measured sample values were normalised to the accepted values of 0.511961 ± 0.000013 (corresponding to 0.511856 for La Jolla (Chauvel and Blichert-Toft, 2001)) for ^{143}Nd/^{144}Nd of the "Rennes" in-house Nd standard and 0.282163 ± 0.000009 for ^{176}Hf/^{177}Hf of the JMC-475 Hf standard using sample-standard bracketing. Mass bias were corrected relative to ^{146}Nd/^{144}Nd = 0.7219 and ^{179}Hf/^{177}Hf = 0.7325 using an exponential law. Total procedural blanks for Sm, Nd, Lu, and Hf were less than 20, 50, 20, and 20 pg, respectively. Isochron calculations (ages, initial isotopic compositions, and MSWDs) were done using a MatLab least-squares software by F. Albarède (version 6.0, 2013). Errors applied to the measured ^{147}Sm/^{144}Nd and ^{176}Lu/^{177}Hf ratios were ± 0.2%, while errors applied to the measured ^{143}Nd/^{144}Nd and ^{176}Hf/^{177}Hf ratios were ± 0.00001, which was the external reproducibility of the present analytical sessions as determined by the repeated standard measurements. In those cases where the in-run error for a sample was larger than the external reproducibility, the in-run error was used for the least-squares regressions. The decay constants used were 6.54×10^{-12} y^{-1} for ^{147}Sm and 1.865×10^{-11} y^{-1} for ^{176}Lu (Scherer *et al.*, 2001). If the decay constant for ^{176}Lu by Söderlund *et al.* (2004) of 1.867×10^{-11} is used, the calculated ages are older by 1 per mil, which is within the error of the measurements. All Sm-Nd and Lu-Hf concentration and isotope data are reported in Table S-5.

b. Al Diffusion Modelling

To model Al diffusion in orthopyroxene, we solved the general diffusion equation,

$$\frac{\partial C}{\partial t} = D(T)\ \frac{\partial^2 C}{\partial x^2} \qquad \text{Eq. S-1}$$

using an explicit finite difference program with adapative time-steps using a VisualBasic Macro in Excel developed by C.-T. Lee. The program is available upon request.

The temperature-dependent diffusion coefficient D follows an Arrhenius relation

$$D = D_0 e^{-E/(RT)} \qquad \text{Eq. S-2}$$

where E is the activation energy (kJ/mol), R the gas constant, T the temperature (K), and D_0 (m^2/s) the diffusion coefficient at infinitely high temperature. We are interested in modelling the exsolution of garnet lamellae in orthopyroxene, a temperature and pressure-dependent process. Al concentration in orthopyroxene in equilibrium with exsolved garnet will thus change at each successive incremental change in temperature and/or pressure. Thus, a boundary condition that accounts for Al concentration in orthopyroxene in equilibrium with garnet (*e.g.*, at the garnet-pyroxene contact) as a function of temperature and/or pressure must be defined in the model. In addition, some assumption of how temperature changes with time must also be specified.

Temperature-dependent boundary condition: Al concentration in orthopyroxene as a function of temperature

Al in orthopyroxene in equilibrium with garnet was parameterised as a function of temperature using the garnet-orthopyroxene thermobarometer of Harley and Green (1982). We assumed that the Fe/Mg ratio in orthopyroxene is roughly constant given that it is buffered by the bulk rock composition and that the exchange coefficient of Fe/Mg between pyroxenes and olivines are close to 1 and relatively insensitive to temperature and pressure (von Seckendorff and O'Neill, 1993). We have also assumed that the Ca in the garnet does not change significantly, being more of a function of the bulk rock composition than on temperature and pressure (Pearson *et al.*, 2003). The parameterised Al concentration in orthopyroxene as a function of T or P is shown in Figure S-6. Al concentration is shown in units of cation fraction X_{Al} on the orthopyroxene M1 site, where X_{Al} = Al/2, and Al is the number of cations in the formula for orthopyroxene on a 6 oxygen basis.

We assumed isobaric cooling at 3 GPa from 1275 °C to 750 °C (we explore different starting temperatures in a later section). The starting temperature of 1275 °C is obtained using a parameterised relationship between Al in orthopyroxene as a function of temperature at a constant pressure of 3 GPa,

$$X_{Al\ (3\ GPa)} = (2.86 \times 10^{-8})T^2 - (3.58 \times 10^{-6})T - 0.0043 \qquad \text{Eq. S-3}$$

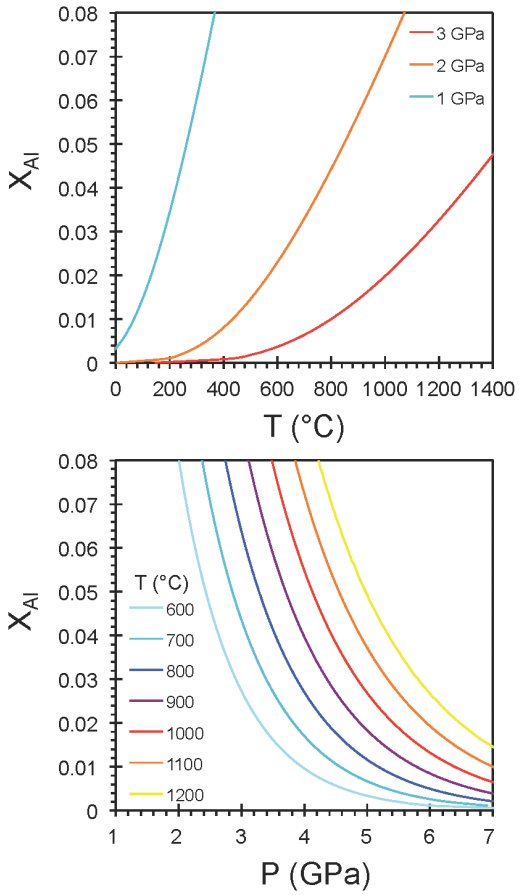

Figure S-6 The thermobarometer of Harley and Green (1982) parameterised as a function of X_{Al} on M1 site of opx versus temperature at constant pressure (top) and X_{Al} on M1 site of opx versus pressure at constant temperature (bottom).

The assumption of isobaric cooling at 3 GPa is a simplified one, since in reality garnet could be exsolving over a range of pressures. However, the effect of cooling temperatures on Al solubility in orthopyroxene is much greater than that of increasing pressure. In addition, the orthopyroxene Al diffusion profiles against garnet lamellae form only after garnet nucleates, which for sample 1026V appears to be at ~3 GPa. We adopted 750 °C as the final temperature based on an average of temperatures obtained from mineral rim pairs in 1026V (Chin *et al.*, 2012).

Temperature-time scenarios, D_0 and E

Case 1: Starting temperature = 1275 °C, final temperature = 750 °C

In our Al diffusion modelling of garnet exsolution lamellae in host orthopyroxene, we evaluated cooling scenarios that followed an exponential decay from an initial temperature T_0 to a final temperature T_f

$$T = T_f + (T_0 - T_f)\, e^{(-t/\tau)} \qquad \text{Eq. S-4}$$

where t is time and τ represents the e-fold characteristic timescale of cooling. Three values of τ were investigated, 3, 7, and 50 Myr. The initial temperature of 1275 °C was chosen to correspond to the maximum Al concentration (at 3 GPa, the final equilibration pressure) where the concentration profile flattens out away from the garnet contact. The final temperature of 750 °C corresponds to the final equilibration temperature recorded by garnet-orthopyroxene pairs in 1026V (Chin *et al.*, 2012). Thus, the initial temperature effectively represents the temperature at which garnet first nucleated and Al in orthopyroxene began diffusing out to support further garnet growth. Alternative cooling scenarios, such as a linear decay, could have also been explored, but exponential decay to a constant final temperature is physically more reasonable.

In Figure S-7 we plot all model results using an activation energy E of 375 kJ/mol, D_0 from 10^{-7} to 10^{-12} m^2/s, and for cooling scenarios using τ of 3, 7, and 50 Myr. We adopt an activation energy of ~375 kJ/mol as recommended by Cherniak and Liang (2007) for diffusion of rare earth elements in orthopyroxene. Cherniak and Liang showed that activation energy is not sensitive to ionic radius, so we assume that the activation energy for Al is similar. Values for the pre-exponent D_0, however, do vary systematically with ionic radius for diffusion of trivalent cations in clinopyroxene, but there is insufficient data to evaluate this dependency on radius in orthopyroxene. For these reasons, we have explored a range of D_0 as shown in Figure S-7. D_0s of 10^{-7} to 10^{-9} m^2/s produce diffusion profiles with much less curvature than observed, indicating that input diffusivities are too high. D_0s of 10^{-11} m^2/s produce too much curvature and diffusion haloes too thin compared to observation, indicating that input diffusivities are too low. We find that D_0 of ~10^{-10} m^2/s best matches the observed curvature. We thus adopt D_0 of 10^{-10} m^2/s for our models.

For completeness, however, we also explored activation energies of 350 and 400 kJ/mol. *E*s of 300 and 400 kJ/mol produce profiles too flat and too steep, respectively. Values of 350 and 375 kJ/mol produce curvatures more consistent with our data, but we nonetheless choose 375 kJ/mol in accordance with Cherniak and Liang.

In Figure S-8 we plot the norm of residuals, defined as $\sqrt{SS_{res}}$, where $SS_{res} = \sum_i (y_i - f_i)^2$, y_i = observed, and f_i = model, for models using 375 kJ/mol and D_0 of 10^{-10} m^2/s for cooling rates with τ = 3, 7, and 50 Ma. The norm of residual for each model at times 0.1, 1, 5, 10, and 20 Ma is plotted. From Figure S-8, the

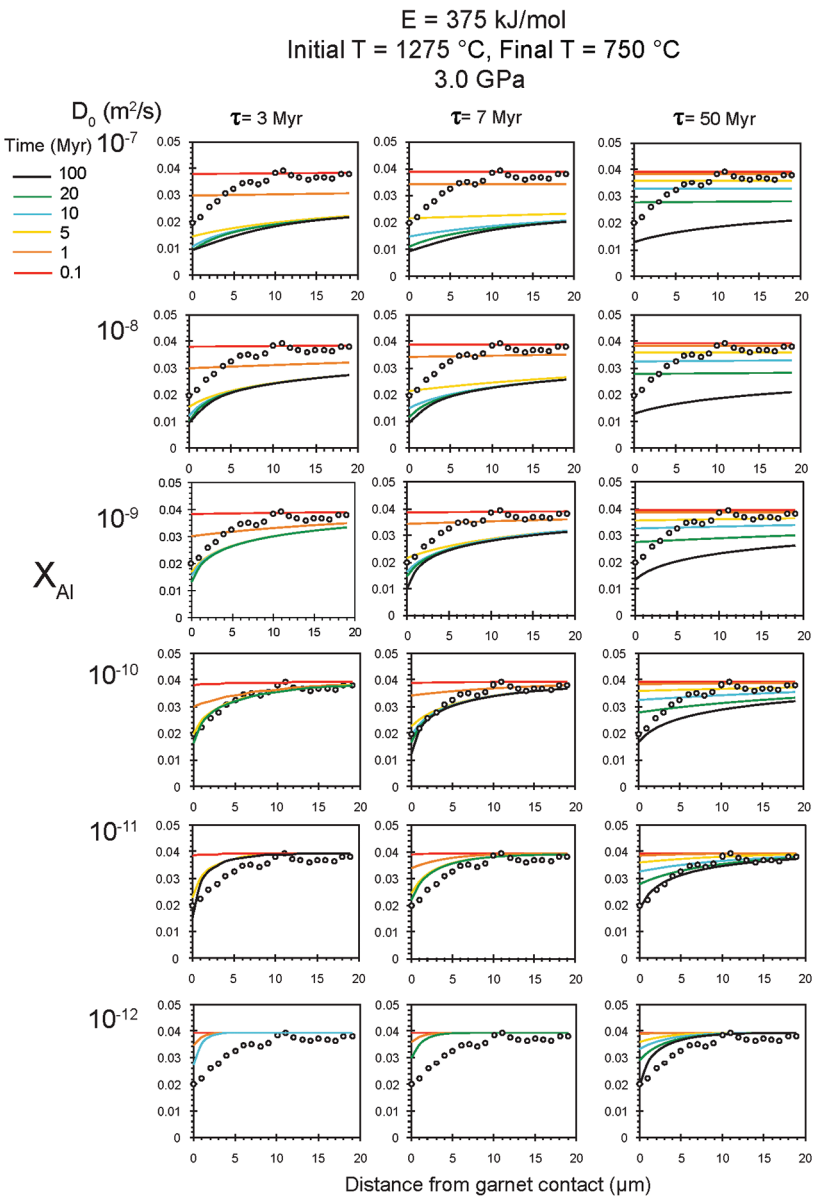

Figure S-7 Modelled Al-diffusion profiles at various times at different values of D_0 and constant E (375 kJ/mol), using starting T = 1275 °C, final T = 750 °C. Each column shows models performed at a different cooling scenario.

lowest norm of residual occurs at a modelled diffusion profile at 5 Myr after cooling from initially hot (1275 °C) conditions and using the most rapid cooling scenario (τ = 3 Ma). It can be seen from Figure S-8 that cooling scenarios of τ = 3 and 7 Myr both reproduce the observed diffusion profiles, but much slower cooling scenarios (τ = 50 Myr) do not.

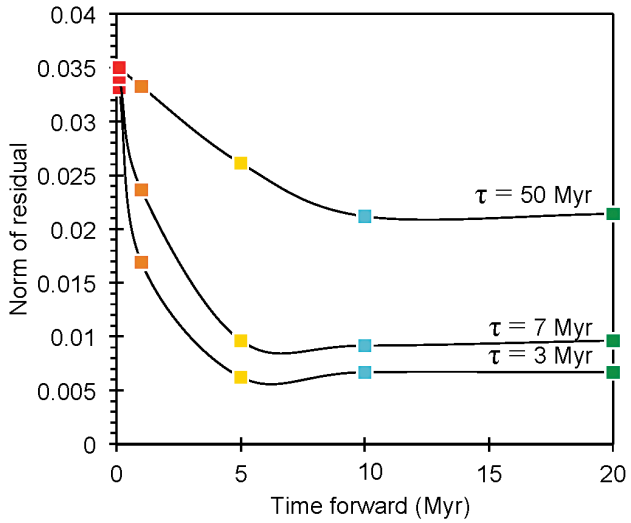

Figure S-8 Norm of residual of Al-diffusion models (E = 375 kJ/mol, D_0 = 10^{-10} m^2/s) at 0.1, 1, 5, 10, and 20 Ma and at different cooling scenarios.

Case 2: Starting temperature = 1100 °C, final temperature = 750 °C

We also explored a second scenario with a lower starting temperature at 1100 °C. This temperature corresponds to the core compositions of the high-MgO garnet websterites, which are interleaved with the garnet peridotites at 3 GPa. Since the websterites are cumulates of primary basaltic liquids, it is probable that they precipitated at temperatures of ca. 1100 to 1200 °C, lower than the residual peridotites which would reflect temperatures corresponding to melt extraction (1250 – 1350 °C). The Al content far from the garnet contact in our modelled transect is 0.039 (in X_{Al} units). Owing to the positive slope in P-T space of Al isopleths for mantle assemblages, at a temperature of 1100 °C, X_{Al} = 0.039 would occur at 2.5 GPa using the Harley and Green (1982) parameterisation scheme discussed above. Keeping all other model parameters constant (E = 375 kJ/mol, τ = 3, 7, 50 Myr, and varyng D_- from 10^{-7} to 10^{-12} m^2/s) and using a starting temperature of 1100 °C, we find that modelled profiles after 5 – 10 Myr at D_0 = 10^{-8} m^2/s and τ = 3 Myr provide consistent fits to the data (Fig. S-9).

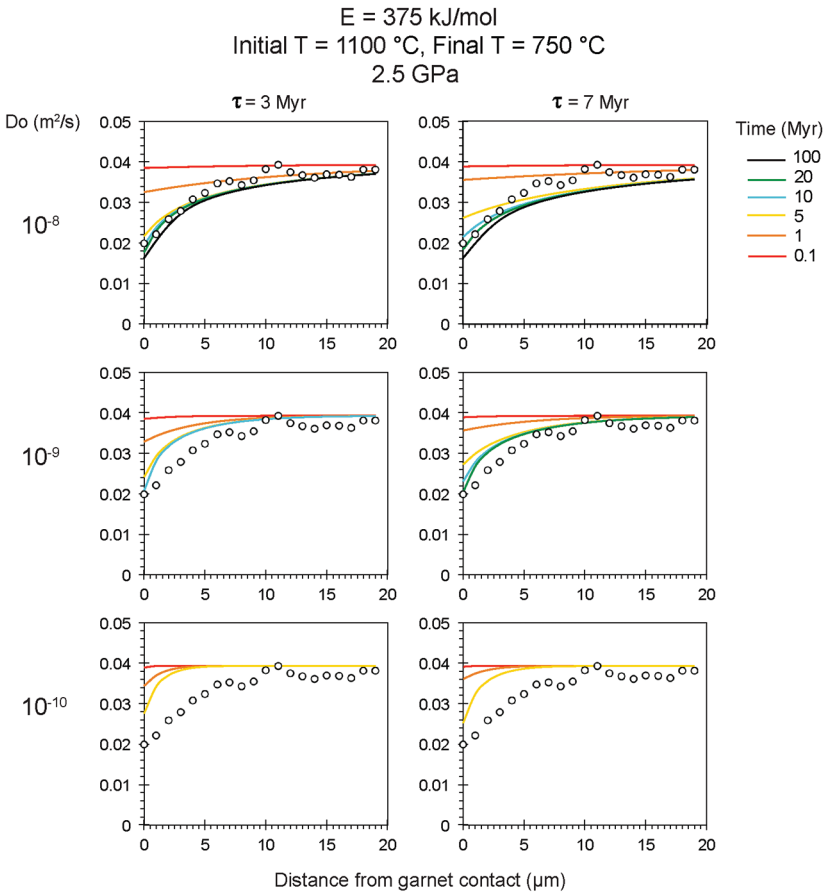

Figure S-9 Modelled Al-diffusion profiles at various times at different values of D_0 and constant E (375 kJ/mol), using starting T = 1100 °C, final T = 750 °C.

Thus, using a lower starting temperature of 1100 °C does not significantly change the results obtained using the higher starting temperature of 1275 °C. Our preferred model is that using 1275 °C, D_0 = 10^{-10} m^2/s, E = 375 kJ/mol, and τ = 3 Myr (*e.g.*, Figs. 2A and S-7), since the norm of residuals for this model is lower (0.0062) compared to the equivalent model (0.0087) using 1100 °C as starting temperature (top left panel in Fig. S-9). However, both scenarios are consistent with rapid cooling within 5-10 Myr at fast cooling rates.

c. Thermal Evolution of Lithosphere

To model the thermal evolution of the lithosphere after impingement on a cold subducting slab, we assumed the thermal evolution is controlled only by conduction. We thus solved the heat diffusion equation using finite-difference (thermal diffusivity was 10^{-6} m^2/s). The lithosphere was assumed to be 100 km thick. For the initial thermal state, we assumed that the temperature was zero at the surface and 1350 °C at the base of the lithosphere and that the temperature within the lithosphere changed gradually between these two boundary values. Temperature between 90 and 99 km was initially held at 1300 °C to reflect the initially hot magmatic conditions associated with peak Sierran arc magmatism. To model the cooling of the lithosphere by impingement against the cold (750 °C) slab, the boundary condition at the base of the lithosphere was instantaneously changed to 750 °C.

Supplementary Information References

Blichert-Toft, J. (2001) On the Lu-Hf Isotope Geochemistry of Silicate Rocks. *Geostandards Newsletter* 25, 41-56.

Blichert-Toft, J., Puchtel, I.S. (2010) Depleted mantle sources through time: Evidence from Lu-Hf and Sm-Nd isotope systematics of Archean komatiites. *Earth and Planetary Science Letters* 297, 598-606.

Blichert-Toft, J., Chauvel, C., Albarède, F. (1997) Separation of Hf and Lu for high-precision isotope analysis of rock samples by magnetic sector-multiple collector ICP-MS. *Contributions to Mineralogy and Petrology* 127, 248-260.

Blichert-Toft, J., Boyet, M., Télouk, P., Albarède, F. (2002) $^{147}Sm/^{143}Nd$ and $^{176}Lu/^{176}$ Hf in eucrites and the differentiation of the HED parent body. *Earth and Planetary Science Letters* 204, 167-181.

Chauvel, C., Blichert-Toft, J. (2001) A hafnium isotope and trace element perspective on melting of the depleted mantle. *Earth and Planetary Science Letters* 190, 137-151.

Cherniak, D.J., Liang, Y. (2007) Rare earth element diffusion in natural enstatite. *Geochimica et Cosmochimica Acta* 71, 1324-1340.

Chin, E.J., Lee, C.-T.A., Luffi, P., Tice, M. (2012) Deep Lithospheric Thickening and Refertilization beneath Continental Arcs: Case Study of the P, T and Compositional Evolution of Peridotite Xenoliths from the Sierra Nevada, California. *Journal of Petrology* 53, 477-511.

Harley, S.L., Green, D.H. (1982) Garnet-orthopyroxene barometry for granulites and peridotites. *Nature* 300, 697-701.

Lee, C.-T.A. (2005) Trace Element Evidence for Hydrous Metasomatism at the Base of the North American Lithosphere and Possible Association with Laramide Low-Angle Subduction. *The Journal of Geology* 113, 673-685.

Lee, C.-T.A., Rudnick, R.L., Brimhall Jr, G.H. (2001) Deep lithospheric dynamics beneath the Sierra Nevada during the Mesozoic and Cenozoic as inferred from xenolith petrology. *Geochemistry Geophysics Geosystems* 2.

Pearson, D., Canil, D., Shirey, S. (2003) Mantle samples included in volcanic rocks: xenoliths and diamonds. *Treatise on Geochemistry* 2, 171-275.

Scherer, E., Münker, C., Mezger, K. (2001) Calibration of the Lutetium-Hafnium Clock. *Science* 293, 683-687.

Söderlund, U., Patchett, P.J., Vervoort, J.D., Isachsen, C.E. (2004) The ^{176}Lu decay constant determined by Lu-Hf and U-Pb isotope systematics of Precambrian mafic intrusions. *Earth and Planetary Science Letters* 219, 311-324.

von Seckendorff, V., O'Neill, H.S.C. (1993) An experimental study of Fe-Mg partitioning between olivine and orthopyroxene at 1173, 1273 and 1423 K and 1.6 GPa. *Contributions to Mineralogy and Petrology* 113, 196-207.

Table SI-1 Major element compositions (wt. %) of orthopyroxene profile in sample 1026V in Figure 1C.

ID	1b#7	1b#8	1b#9	1b#10	1b#11	1b#12	1b#13	1b#14	1b#15	1b#16	1b#17	1b#18	1b#19	1b#20	1b#21	1b#22	1b#23	1b#24	1b#25	1b#26
X mm	32.2384	32.2394	32.2404	32.2414	32.2424	32.2434	32.2444	32.2454	32.2464	32.2474	32.2484	32.2494	32.2504	32.2514	32.2524	32.2534	32.2544	32.2554	32.2564	32.2574
Y mm	26.0977	26.0972	26.0987	26.0982	26.0997	26.0992	26.1007	26.1002	26.1017	26.1012	26.1027	26.1022	26.1037	26.1032	26.1047	26.1042	26.1057	26.1052	26.1067	26.1062
at contact with garnet lamella																				
SiO_2	57.53	57.37	57.13	56.86	57.44	57.00	56.97	57.10	57.22	57.03	56.59	56.41	56.65	57.25	56.90	57.20	57.16	57.08	56.77	56.57
TiO_2	0.013	0.022	0.028	0.002	0.014	0.005	0.035	0.035	0.017	0.023	0.01	0.019	0.023	0.005	0	0.024	0.029	0.023	0.029	0.001
Al_2O_3	0.99	1.09	1.27	1.37	1.52	1.60	1.71	1.74	1.69	1.74	1.85	1.88	1.84	1.82	1.78	1.83	1.82	1.79	1.88	1.87
Cr_2O_3	0.31	0.29	0.35	0.47	0.49	0.60	0.65	0.50	0.55	0.54	0.57	0.50	0.51	0.43	0.58	0.42	0.37	0.52	0.36	0.47
FeOT	5.84	5.58	5.45	5.39	5.34	5.45	5.64	5.75	5.52	5.48	5.68	5.74	5.64	5.68	5.36	5.68	5.53	5.74	5.83	5.91
MnO	0.16	0.10	0.11	0.13	0.09	0.16	0.14	0.09	0.15	0.10	0.11	0.11	0.08	0.05	0.13	0.11	0.08	0.11	0.14	0.12
MgO	35.28	34.91	34.90	34.65	34.71	34.79	34.58	34.63	34.64	34.26	32.57	31.76	34.50	34.95	34.69	34.69	34.71	34.56	34.55	34.47
CaO	0.10	0.10	0.11	0.13	0.14	0.13	0.13	0.11	0.12	0.12	0.11	0.14	0.12	0.11	0.11	0.11	0.11	0.11	0.11	0.13
Na_2O	0.022	0.032	0.007	0.007	0.003	0.007	0.001	0	0.009	0.015	0.011	0.007	0.011	0.026	0	0.023	0	0	0	0.005
NiO	0.06	0.10	0.07	0.06	0.02	0.06	0.05	0.08	0.06	0.07	0.02	0.08	0.17	0.10	0.01	0.14	0.14	0.05	0.14	0.08
Total	100.29	99.59	99.42	99.06	99.76	99.79	99.91	100.04	99.98	99.38	97.51	96.65	99.54	100.42	99.56	100.21	99.94	99.98	99.80	99.61

Geochem. Persp. Let. (2015) 1, 20-32 | doi: 10.7185/geochemlet.1503

Table SI-2 Orthopyroxene major element compositions (wt. %) in Sierran garnet pyroxenites.

	BC98-7				BC98-5					
ID	BC987_01-opxR	BC987_02-opxC	BC987_07-opxR	BC987_08-opxC	BC985_03-opxR	BC985_04-opxC	BC985_07-opxR	BC985_08-opxC	BC985_17-opxR	BC985_18-opxC
	rim	core	rim	core	rim	core	rim	core	rim	core
x (µm)	12871	12793	657	273	3731	3919	-122	-96	7631	7345
y (µm)	13416	13785	8599	8825	23191	23429	26133	25878	27889	27423
SiO_2	54.13	54.29	54.94	54.10	55.19	54.64	55.12	54.47	54.86	53.72
TiO_2	0.043	0.02	0.034	0.02	0.02	0.013	0	0.034	0.028	0.01
Al_2O_3	1.80	1.99	1.50	2.05	0.74	1.22	0.76	1.49	0.92	1.68
Cr_2O_3	0.13	0.11	0.10	0.20	0.08	0.11	0.08	0.09	0.08	0.11
FeOT	12.80	12.85	12.92	13.07	12.32	12.38	12.71	13.14	13.19	13.55
MnO	0.14	0.14	0.17	0.15	0.11	0.11	0.11	0.15	0.16	0.16
MgO	30.80	30.57	31.14	30.76	31.45	31.07	31.32	30.45	30.53	30.18
CaO	0.25	0.21	0.20	0.16	0.12	0.17	0.10	0.19	0.20	0.20
Na_2O	0.014	0.025	0.014	0.017	0.012	0.002	0.005	0.012	0.006	0
Total	100.09	100.22	101.02	100.53	100.04	99.70	100.21	100.02	99.98	99.61

Geochem. Persp. Let. (2015) 1, 20-32 | doi: 10.7185/geochemlet.1503

Table SI-3 Clinopyroxene major element compositions (wt. %) in garnet pyroxenites.

	BCX			BC98-7				BC98-5					
ID	BCX_03-cpx	BCX_05-cpx	BCX_08-cpx	BC987_05-cpxR	BC987_06-cpxC	BC987_09-cpxR	BC987_10-cpxC	BC985_05-cpxR	BC985_06-cpxC	BC985_11-cpxR	BC985_12-cpxC	BC985_15-cpxR	BC985_16-cpxC
	rim next to gt	rim next to gt	rim next to gt	rim	core	rim	core	rim	core	rim	core	rim	core
x (µm)	-6	-5075	-4444	12686	12656	769	849	4675	5089	-470	-299	7454	8124
y (µm)	-15851	-6058	-13636	14152	14420	8874	9171	23847	24479	26791	27289	28170	28080
SiO_2	54.85	54.80	54.53	53.79	53.62	54.45	53.86	54.35	53.59	54.31	53.41	54.06	52.98
TiO_2	0.18	0.19	0.21	0.15	0.24	0.09	0.14	0.05	0.15	0.05	0.13	0.04	0.13
Al_2O_3	9.34	9.42	9.24	3.91	4.49	3.56	4.03	1.97	4.19	2.32	4.42	1.66	4.70
Cr_2O_3	0.04	0.00	0.00	0.44	0.44	0.45	0.44	0.26	0.22	0.27	0.29	0.26	0.36
FeOT	4.14	4.17	4.19	3.73	4.04	3.50	3.65	3.60	4.18	3.59	4.22	3.48	4.37
MnO	0.002	0.029	0.037	0.084	0.056	0.033	0.037	0.076	0.098	0.037	0.051	0.041	0.057
MgO	10.57	10.57	10.60	15.00	14.50	15.16	14.96	16.17	14.77	16.03	14.73	16.37	14.41
CaO	17.04	16.76	16.97	21.81	21.38	21.83	21.61	23.22	21.97	22.95	22.12	23.25	22.08
Na_2O	4.61	4.70	4.53	1.61	1.67	1.65	1.71	0.90	1.23	1.03	1.36	0.79	1.36
Total	100.78	100.64	100.30	100.51	100.44	100.72	100.44	100.59	100.40	100.58	100.72	99.93	100.46

Geochem. Persp. Let. (2015) 1, 20-32 | doi: 10.7185/geochemlet.1503

Table SI-4 Garnet major element compositions (wt. %) in Sierran garnet pyroxenites.

	BC98-5						BCX						BC98-7			
ID	BC985_01-GT1	BC985_02-GT1	BC985_09-GTr	BC985_10-GTc	BC985_13-GTc	BC985_14-GTr	BCX_01-GTC	BCX_02-GTr	BCX_04-GTr	BCX_06-GTr	BCX_07-GTC	BCX_09-GT	BC987_03-GTC	BC987_04-GTr	BC987_11-GT1	BC987_12-GT2
			rim	core	core	rim	core	rim	rim	rim	core		core	rim		
x (µm)	3639	3671	-308	-593	7284	7366	3793	8008	338	-4877	-4680	-4976	11863	12152	57	60
y (µm)	22892	22835	26127	26358	28034	28111	-12444	-12849	-16003	-5904	-5797	-13521	13995	13891	9855	9811
SiO_2	40.15	40.13	40.01	40.23	39.77	40.00	39.35	39.16	39.31	39.08	39.05	39.19	40.23	40.30	40.28	39.96
TiO_2	0.044	0.093	0.048	0.104	0.104	0.017	0.14	0.073	0.16	0.05	0.107	0.093	0.077	0.053	0.062	0.058
Al_2O_3	22.94	22.86	22.84	22.62	22.58	22.60	22.20	22.10	22.56	22.58	22.25	22.46	22.72	22.90	22.84	22.81
Cr_2O_3	0.34	0.37	0.42	0.34	0.39	0.38	0	0.04	0	0.03	0.02	0.02	0.47	0.52	0.51	0.49
FeOT	18.00	18.16	18.97	18.09	18.94	19.20	22.73	21.14	20.73	20.69	20.96	20.74	17.93	18.79	18.45	18.43
MnO	0.56	0.57	0.53	0.42	0.54	0.57	0.66	0.56	0.53	0.56	0.53	0.60	0.56	0.57	0.53	0.57
MgO	13.10	12.94	12.31	12.81	12.28	12.14	9.43	7.41	7.95	7.40	7.48	7.36	13.42	12.70	13.14	13.21
CaO	5.61	5.61	5.61	5.65	5.51	5.50	6.26	9.89	9.58	10.38	10.17	10.46	5.19	5.22	5.22	5.29
Na_2O	0.02	0.025	0.014	0.02	0.005	0.019	0.056	0.024	0.067	0.003	0.039	0.02	0.014	0.012	0.02	0.002
Total	100.76	100.75	100.75	100.27	100.11	100.42	100.82	100.41	100.88	100.77	100.60	100.94	100.62	101.07	101.05	100.81

Geochem. Persp. Let. (2015) 1, 20-32 | doi: 10.7185/geochemlet.1503

Table SI-5 Sm-Nd and Lu-Hf concentrations and isotope compositions of Sierran pyroxenites.

Sample	Sm (ppm)	Nd (ppm)	$^{147}Sm/^{144}Nd$	$^{143}Nd/^{144}Nd$	2σ	Lu (ppm)	Hf (ppm)	$^{176}Lu/^{177}Hf$	$^{176}Hf/^{177}Hf$	2σ
BC98-7 gt	0.563	0.295	1.152	0.513068	0.000008	0.455	0.0852	0.7581	0.283596	0.000044
BC98-7 cpx	2.00	6.50	0.1858	0.512566	0.000004	0.00628	0.912	0.0009766	0.282737	0.000005
BC98-7 wr	0.769	2.13	0.2178	0.512562	0.000004	0.134	0.360	0.05285	0.283094	0.000005
BC98-5 kgt	0.727	0.533	0.8257	0.512877	0.000006	0.769	0.186	0.5871	0.283728	0.000014
BC98-5 cpx	2.34	6.51	0.2173	0.512526	0.000005	0.00946	1.07	0.001252	0.282716	0.000004
BC98-5 wr	1.48	4.04	0.2215	0.512523	0.000005	0.158	0.817	0.02749	0.282841	0.000014
BCX gt	3.50	2.19	0.9639	0.512956	0.000005	1.22	0.344	0.5037	0.283774	0.000010
BCX gt dupl						1.25				
BCX cpx	1.11	1.80	0.3718	0.512630	0.000012	0.0197	1.10	0.002529	0.282767	0.000003
BCX cpx dupl						0.0197	1.09	0.002574		
BCX wr	2.79	4.73	0.3563	0.512702	0.000004	0.514	0.936	0.07795	0.282913	0.000004

gt = garnet
cpx = clinopyroxene
wr = whole-rock
kgt = kelyphite-rimmed garnet